Sand Deformation Mechanisms

Mobilised with Active Retaining Wall Movement

C. Deng and S.K. Haigh

ABSTRACT

A series of centrifuge tests was conducted to explore the deformation mechanisms mobilised in loose and dense sand for a complete set of active rigid retaining wall movement modes: rotation about the base and top and translation. The sand deformation was measured by particle image velocimetry and data of displacements and strains are reported. A simplified deformation mechanism is proposed for sand behind a rigid wall rotating about the top and validated with the centrifuge test results. The paper reveals that the sand deformation caused by wall translation can be well characterised by the superposition of mechanisms with equal but opposite wall rotation about the top and base. Integration of these displacement mechanisms together with a constitutive law into an equilibrium solution for wall bending would allow designers to predict deformations during construction as well as ultimate collapse.

KEYWORDS: centrifuge modelling, deformation, retaining walls, sands, strain

INTRODUCTION

Research on retaining walls has been conducted for over 300 years since Gautier (1717), a French royal engineer, carried out experiments aiming to formulate a design procedure for

retaining walls. The vast majority of work in the last three centuries has focused on the earth pressures acting on the retaining wall, which have been analytically deduced (Coulomb, 1776, Rankine, 1857), numerically calculated (Potts and Fourie, 1986, Chang and Chao, 1994) and experimentally monitored (Rowe and Peaker, 1965, Fang and Ishibashi, 1986, Fang et al., 1994). This focus on earth pressures is to be expected, as they allow stability calculations to be performed, however they do not allow calculation of pre-failure deformations. In order to calculate wall movements, the soil deformation mechanism must be evaluated. Historically, this was not explored as much as earth pressures, as analytical solutions are not able to accurately predict the strain field behind retaining walls.

Direct measurements of soil deformation behind retaining walls began with the work of Roscoe (1963) using X-ray radiography to monitor the sand displacement with rigid wall movement, with Bransby and Milligan (1975) extending this technique to observe the behaviour of flexible walls in sand. Bolton and Powrie (1988) then extended the result of Bransby and Milligan (1975) to clay with an assumption that zero dilation satisfies the undrained behaviour of clay and proposed the simplified admissible strain fields in clay compatible with a complete set of wall movement as shown in Figure 1. Bolton and Powrie (1988) also stated that the wall roughness had a negligible effect on the strain fields which emerged in model experiments.

Figure 1. Admissible strain fields for (a) wall rotation about the base; (b) wall rotation about the top; (c) wall translation (Bolton and Powrie (1988))

The simplified admissible strain field behind a frictionless rigid wall rotating outwards by a small angle of $\delta\theta$ about its base is shown in Figure 1(a). The horizontal, vertical and shear strain increments are assumed to be uniform within the deforming wedge *AVO* with values being given by Equations 1-3.

$$\delta\varepsilon_h = -\delta\theta \quad (1)$$

$$\delta\varepsilon_v = +\delta\theta \quad (2)$$

$$\delta\gamma = 2\delta\theta \quad (3)$$

where $\delta\theta$ is the wall rotation angle increment (radian), $\delta\varepsilon_h$, $\delta\varepsilon_v$ and $\delta\gamma$ are the horizontal, vertical and shear strain increments (taking compression positive).

The admissible strain field compatible with wall rotation about the top is depicted in Figure 1(b), in which the triangle *AVO* is assumed to be rigid while the wedge *ABO* deforms with strain increments being also calculated by Equations 1-3.

Bolton and Powrie (1988) also developed a hypothesis that the admissible strain field caused by a frictionless rigid wall translating outwards by a small distance can be determined by the superposition of those compatible with equal but opposite wall rotation about the base and top. A square strain field with uniform strain increments being given by Equations 4-6 was then proposed in Figure 1(c).

$$\delta\varepsilon_h = -\frac{\delta u}{h} \quad (4)$$

$$\delta\varepsilon_v = +\frac{\delta u}{h} \quad (5)$$

$$\delta\gamma = 2\frac{\delta u}{h} \quad (6)$$

where δu is the horizontal translational wall displacement increment and h is the wall height.

Advances in computer vision techniques have made optical tracking of soil behind a window an attractive technique for studying plane-strain deformations. White et al. (2003) implemented particle image velocimetry (PIV), a technique originally developed for a velocity-measurement in fluid mechanics (Adrian, 1991), in a manner suited to the analysis of geotechnical tests and

developed a MATLAB module, GeoPIV, which can measure the movement of a fine mesh of soil patches with a high precision. This has since been further developed by Stanier et al. (2015) with the measurement precision being improved significantly.

Niedostatkiewicz et al. (2011) conducted a series of 1g tests to analyse shear zone development with movement of a 170 mm high retaining wall utilising GeoPIV and compared the results with those from finite element modelling and tests conducted by Arthur (1962), Bransby (1968), Lord (1969) and Smith (1972). Deformation patterns measured with GeoPIV were shown to be similar to those observed previously using X-rays. These experiments, however, suffer from their low stress level; the largest wall involved in all the tests mentioned was 330 mm high, and hence existed at a stress level far below that of field retaining walls. As the constitutive behaviour of soils will govern the deformation pattern observed, the low stress level and subsequent excessive dilatancy will cause errors in the prediction of full-scale behaviours.

Diakoumi & Powrie (2013) and Deng et al. (2019) described a method for the design of flexible retaining walls in clay which takes into account the pre-failure deformations of wall and soil. In order to do this, a linkage is needed between the wall movements and soil strains, which, together with a constitutive model linking soil strains and stresses allows an equilibrium wall configuration to be obtained for any wall geometry. This paper describes the use of particle image velocimetry in centrifuge tests simulating a complete set of active movements of a rigid retaining wall to visualise and model the sand deformation mechanisms mobilised with different wall movement modes. The mechanisms developed can then be superposed within the design method. The use of centrifuge modelling allows correct stress levels to exist within the small-scale model and the results are shown to differ from those obtained from conventional

1g tests, especially in dense sand. While all small-scale models suffer due to boundary conditions, especially friction along the plane-strain boundaries, this data provides a strong foundation for a future design process.

EXPERIMENTAL SET-UP

Six centrifuge tests were conducted to explore the sand deformation mechanisms mobilised with different wall movement modes, i.e. rotation about the base, translation and rotation about the top. Each test was replicated in both loose and dense sand. All the tests were carried out at 40g using the Turner beam centrifuge (Schofield, 1980). Test designations are shown in Table 1.

Table 1. Summary of test configurations

Test ID	Wall movement type	Sand density	Wall displacement
CD01	Rotation about the base	Loose (37%)	2.0% *H*
CD02	Rotation about the base	Dense (82%)	1.0% *H*
CD03	Translation	Loose (33%)	1.0% *H*
CD04	Translation	Dense (85%)	1.0% *H*
CD05	Rotation about the top	Loose (36%)	2.0% *H*
CD06	Rotation about the top	Dense (87%)	0.25% *H*

The models were constructed in a 780 mm wide, 560 mm high and 200 mm thick container with a transparent Perspex window shown schematically in Figure 2(a). The surface of the steel back plate was plated with polished hard chrome and a PTFE plate was situated on the container bottom to minimise friction. The Perspex window in the front was polished before every test in order to both reduce friction and offer a clear visual field for deformation measurement.

Figure 2. (a) Schematic diagram of experimental set-up; (b) Unprocessed images captured simultaneously

An aluminium retaining wall, with a thickness of 10 mm (0.4 m at prototype scale) and a width of 200 mm (8 m at prototype scale), is stiffened by four L shaped steel angles (25.4 mm * 25.4 mm * 3.2 mm) along its height. The retaining wall has an equivalent bending stiffness of 2.4 GNm^2/m at prototype scale and can be regarded as rigid during the tests. Layers of props at two heights were used to control the wall displacement, with individual layers of props being retracted to cause rotation and all props being retracted to cause translation (Deng and Haigh, 2018). It should be noted that the retaining wall has an effective height of 250 mm (10 m at prototype scale) between the two layers of props about which the wall rotates but extends to the container bottom and top. An extra 40 mm thick sand layer (1.6 m at prototype scale) existed below the bottom layer of props. The extended wall top was connected to a horizontal plate to prevent any rotation during the translation tests.

Dry Hostun sand with geotechnical properties shown in Table 2 was pluviated into the container using an automatic sand-pouring machine (Madabhushi et al., 2006) allowing precise control of sand density. A series of confined consolidated-drained compressive triaxial tests was carried out on loose and dense Hostun sand following the ASTM standard procedure (ASTM, 2011) with results being shown in Figure 3 and Table 3. In order to evaluate applicable strength and dilatancy parameters for the model, confining stresses of 40 kPa, 100 kPa and 160 kPa, equivalent to the vertical earth pressures at depths of 2.5 m, 6.5 m and 10 m, were applied to both loose and dense samples. It can be seen that the sand shows a peak friction angle in triaxial conditions of between 29.8° and 46.2°, following the expected trends of increasing with relative density and decreasing with confining stress. Corresponding peak friction angles predicted through the variable-ϕ analysis (Lau and Bolton, 2011), which is an update of the correlation proposed by Bolton (1986), are also included in Table 3 and shown to be similar to

measured values. Although there are kinematic differences between triaxial and plane-strain testing conditions, Schanz and Vermeer (1996) pointed out a fact that the same dilation angle would be measured in both triaxial and plane-strain tests, as implied by the data presented by Bolton (1986). The dilation angles shown in Table 3 can be therefore used for plane-strain analysis. The peak friction angle measured in triaxial tests is, however, smaller than that obtained in plane-strain conditions (Bolton, 1986) and the corresponding differences are calculated as 1.1° and 5.6° for loose and dense Hostun sand, respectively. Additionally, a number of direct shear tests were conducted to measure the interface friction angles between the retaining wall and sand under different vertical confining stresses. The results show that the interface friction angle is approximately constant with confining stress, so average values of 21.7° and 24.7° are adopted for loose and dense sand, respectively.

Table 2. Geotechnical properties of Hostun sand

Item	Symbol	Value	Unit
Maximum void ratio	$e_{\max}$	1.010	-
Minimum void ratio	$e_{\min}$	0.555	-
Specific gravity of solid	G_s	2.65	-
Average particle size of sand (Haigh et al 2012)	d_{50}	470	μm

Figure 3. Stress-strain curves of Hostun sand

Table 3. Strength and dilatancy parameters of Hostun sand

Test configuration	Triaxial peak friction angle, ϕ_p (°)	Critical friction angle, ϕ_{crit} (°)	Peak dilation angle, ψ_p (°)	Predicted triaxial peak friction angle, $\phi_{p,p}$ (°)
Loose (40)	33.0	-	2.2	-
Loose (100)	31.8	-	2.1	-
Loose (160)	29.8	-	2.3	-
Dense (40)	46.2	34.3	18.4	44.9
Dense (100)	44.9	34.0	16.6	42.4
Dense (160)	41.1	33.4	14.7	41.0

Two cameras stood in front of the window and recorded sand deformations with wall movement at an acquisition frequency of 0.25 Hz during the tests. It can be seen from Figure 2 that the images from the two cameras, which shot an overlapping area of the sand, were stitched to create an entire field of view. GeoPIV-RG was used to calculate and analyse the sand deformation mechanism and wall movement. GeoPIV-RG works on the principle of dividing an image into subsets and tracking them from one image to the next with displacements and hence strains being calculated. Subsets with a dimension of 80 × 80 pixels and a spacing of 40 pixels were used for calculation in this research and each subset contained 246 sand particles roughly. Stanier et al. (2015) suggested that one sand particle should cover a minimum area of 4×4 pixels in the image in order to retain enough information and reduce vermiculate artefacts in strain fields. An average area of 5.1×5.1 pixels was covered by one particle in the images recorded during centrifuge tests. According to the precision analysis conducted by Stanier et al. (2015), the shear strain errors were calculated as ~0.1% and ~1% at shear strains of 10% and 100%, respectively, which are acceptable for the deformation analysis. Unless otherwise stated, all the strain distributions plotted in this paper are cumulative from the beginning of the wall displacement process. The wall displacements measured by GeoPIV-RG are compatible with values from LVDTs.

The centrifuge test procedure began by increasing the g-level to 40. The wall was then moved in the desired mode, rotation or translation, by retracting the pistons, allowing the active earth pressures to drive the wall displacement. The retaining wall displacements induced in the six tests are presented in Table 1, in which the normalised wall displacement is the ratio of the maximum horizontal displacement of the wall to the wall height. This may occur at either the wall base or top dependent on the deformation mode.

SAND DEFORMATIONS WITH WALL ROTATION ABOUT THE BASE

With the higher props being retracted and the lower fixed, the rigid retaining wall was rotated about its base. In loose sand, as can be seen from Figure 4(a), a triangular wedge at an approximate angle of 45° to the horizontal forms behind the wall, in which displacement increases towards the wall head. It can be also seen from the vectorial displacement distribution that horizontal displacements are approximately equal to vertical displacements throughout the wedge, showing sand grains moving towards the lower-right direction simultaneously with wall rotation about the base. The shear strain within this wedge is approximately uniform as shown in Figures 4(c) and 4(d), in agreement with the mechanism proposed by Bolton and Powrie (1988), and the geometry of the mechanism remains almost constant with increasing wall displacement. Contractile volumetric strain prevails in the majority of the wedge as shown in Figure 4(b) owing to the initial low relative density of sand, however, dilative volumetric strain occurs in a small region immediately behind the wall. Such a dilative behaviour is in accordance with the triaxial test results on loose Hostun sand as shown in Figure 3. This may also be due to the support provided to this region by friction on the rough retaining wall, which reduces vertical effective stresses close to the wall making sand more dilative. A complete calculation shows the pattern of volumetric strain remaining constant with wall displacements with only the magnitude changing (Deng, 2020).

Figure 4. Loose sand deformation mobilised with wall rotation about the base: (a) vectorial displacement (scale=5); (b) volumetric strain (%); (c) and (d) maximum shear strain (%)

The distributions of maximum shear strain at wall displacements of 0.4% H and 2% H are shown in Figures 4(c) and 4(d), respectively. The average values of volumetric and shear strains within this deforming wedge were calculated. The average volumetric strain in the wedge is 0.14%, showing the absence of any substantial dilation in the sand as a whole and

hence the applicability of Equation 3. The shear wedges in Figures 4(c) and 4(d) are very similar to the predicted triangular strain field in Figure 1(a), once account is taken of the area close to the wall in which no strains were measured due to the meshing process conducted by GeoPIV-RG. If the shear wedges are extrapolated into the lost area, the bases of the wedges intercept the wall at a depth of 9.6 m, just above the point of rotation. The arithmetic averages of the measured shear strain values in the wedges were found to be 0.84% and 4.02% (the RMS values being 0.89% and 4.20%) which are also well predicted by Equation 3 with the calculated values being 0.80% and 4.00%, respectively, validating the strain field proposed by Bolton and Powrie (1988).

Calculating shear strain through the entire image sequence shows that the distribution of maximum shear strain remains self-similar, the average strain value being shown to increase linearly with the wall displacement. A linear relationship between the average maximum shear strain in the shear wedge and the wall rotational displacement can be proposed as Equation 7, identical to Equation 3 (Bolton and Powrie, 1988) for small angles.

$$\overline{\gamma_{max}} = 2\frac{\Delta}{H} \tag{7}$$

where $\overline{\gamma_{max}}$ is the average maximum shear strain, Δ is the wall top displacement during rotation about the base and H is the wall height.

Figure 5 shows the deformation mechanism for wall rotation about the base in dense sand, the final displacement for which is only half that in loose sand as the active state is achieved at lower displacement. It can be seen from Figure 5(a) that the displacement field for dense sand is similar to that for loose sand, but with a substantially steeper wedge. It is worth noting that horizontal displacements of sand grains are higher than vertical displacements, primarily due to dilation of the dense sand. Figure 5(b) shows that the sand accumulates an average dilative

volumetric strain of -0.58% in the wedge during the rotation process, 6.5 times that in loose sand at comparable wall displacements.

The distributions of maximum shear strain mobilised with wall top displacements of 0.2% *H* and 1% *H* are presented in Figures 5(c) and 5(d), respectively. A calculation for the entire image sequence indicates that the shear wedge maintains a right triangular shape. The wedge height will increase to 9 m and thus be close to the wall height if compensation is made for the lost area during GeoPIV-RG calculation. The average shear strain in the wedge increases linearly with the wall rotational displacement but is slightly higher than that predicted by Equation 7.

Figure 5. Dense sand deformation mobilised with wall rotation about the base: (a) vectorial displacement (scale=10); (b) volumetric strain (%); (c) and (d) maximum shear strain (%)

It can be seen from Figure 5(b) that Equation 3 is not applicable for predicting strains in dense sand as there is substantial dilation. Bransby (1972) proposed a kinematically admissible soil strain field compatible with outward wall rotation and validated it through a series of tests involving a laboratory-scale retaining wall (Bransby and Milligan, 1975). The simplest case causing such a field is soil shearing with wall rotation about the base as shown in Figure 6. It is assumed that soil below the triangular wedge *AVO* is always rigid and the dilation angle, ψ, is constant throughout the wedge. The hypotenuse *OA* forms an angle of $45° + \frac{\psi}{2}$ to the horizontal and the increments of shear and volumetric strains within the wedge are given by Equations 8 and 9, respectively.

$$\delta\gamma = 2\,\delta\theta \sec\psi \tag{8}$$

$$\delta\varepsilon_{vol} = -2\,\delta\theta \tan\psi \tag{9}$$

where $\delta\gamma$ is the shear strain increment, $\delta\varepsilon_{vol}$ is the volumetric strain increment (taking dilation negative), $\delta\theta$ is the wall rotation angle increment (radian) about the base and ψ is the dilation angle.

Figure 6. Shear wedge compatible with wall rotation about the base

Assuming the soil behaviour to be approximated by a triaxial test at a confining stress of 100 kPa (the vertical earth pressure at 6.5 m depth), the peak dilation angle can be seen from Table 3 to be 16.6°. However, the dilation angle depends on the strain level so values should be calculated according to the strains mobilised with wall movement. The average measured shear strains within the wedge are 0.41% and 2.13% for wall displacements of 0.2% *H* and 1% *H*, respectively, with the average measured volumetric strains at the same instants being -0.05% and -0.63%, respectively. The corresponding dilation angles at wall displacements of 0.2% *H* and 1% *H* are calculated from the triaxial measurements as 0 and 16.4°, respectively. The average shear strains are therefore well predicted by Equation 8 with calculated values of 0.40% and 2.08%, respectively, the average volumetric strains also being well estimated by Equation 9 with calculated values of 0 and -0.59%, respectively. It can be seen from Figures 5(c) and 5(d) that the hypotenuse of the wedge forms an inclination angle to the horizontal increasing from 47.0° to 54.0°, which is approximately described by $45° + \frac{\psi}{2}$. The kinematically admissible strain field proposed by Bransby (1972) is able to offer a good prediction of behaviour not only for dense sand but also for loose sand utilising a dilation angle of zero.

SAND DEFORMATIONS WITH WALL TRANSLATION

The retaining wall can be translated by retracting all the pistons in the actuator system. As the wall translates, it can be seen from Figure 7(a) that an approximately-triangular rigid block behind the wall slides down a shear plane at an inclination angle of 54.0° to the horizontal. The observed rigid sand block validates the assumption made by Coulomb (1776) of a rigid soil mass sliding upon a shear surface. The measured inclination angle is well predicted by Equation 10 (Mayniel, 1808) with a calculated value of 55.3° considering wall friction based on the Coulomb's solution. It is worth noting that the values of the friction angle incorporated into the calculations are corrected from the triaxial to plane-strain condition.

$$\theta_{\mathrm{inc}} = \tan^{-1}\left[\tan\phi + \sec\phi\sqrt{\frac{\tan\phi}{\tan(\phi+\delta)}}\right] \quad (10)$$

where θ_{inc} is the inclination angle of the sliding surface, ϕ is the sand friction angle and δ is the interface friction angle between sand and the wall.

Figure 7. Loose sand deformation mobilised with wall translation: (a) vectorial displacement (scale=5); (b) volumetric strain (%); (c) and (d) maximum shear strain (%)

More detailed analysis of Figure 7 shows the shear zone to actually be slightly curved and to have a finite thickness as shown in Figures 7(c) and 7(d), which present the maximum shear strains mobilised with translational wall displacements of 0.2% *H* and 1% *H*, respectively. The shear band previously observed for active translation at 1g by Lesniewska et al (2012) was straighter as with lower body forces the change in dilatancy across the height of the model is small, whereas in the centrifuge and at full-scale, self-weight leads to a substantial reduction in dilatancy with depth. A calculation for the entire image sequence indicates that the average slope of the shear zone increases gradually from 45° in the early stages to around θ_{inc}. This demonstrates that the theories proposed by Coulomb (1776) and Mayniel (1808) can only be

used for describing the ultimate limit state. The calculation also shows that the shear zone consists of two parts. A primary part exists across the whole depth with an inclination angle changing from 45° to θ_{inc} induced by global movement of the rigid block and approximately described by the Coulomb's theory. Additionally, a secondary part with higher strain values originates from the wall base with an inclination angle of 45°+ϕ to the horizontal when the wall moves more than 0.1% *H* and local collapse then occurs behind the wall.

A series of incremental maximum shear strain distributions is shown in Figure 8, illustrating the initiation and propagation of the shear zone with wall translation. It can be seen from Figure 8(a) that initially a diffuse primary shear band runs through the whole depth with an inclination angle of 45°. As wall movements increase a localised secondary shear band with a thickness of 15 d_{50}, in accordance with the results presented by Mühlhaus and Vardoulakis (1987), initiates at the base of the wall and propagates upwards. At large displacements, as shown in Figures 8(c) and 8(d), the diffuse primary shear band inclines at θ_{inc} to the horizontal and large shear strains are mobilised in the localised secondary shear band inclining at 45°+ϕ to the horizontal. This is also revealed by coincidence of peak strain values at all depths before the wall translates 0.1% *H* as shown in Figure 9(a). Local collapse with dramatically increasing strains initiates with further wall displacements at the wall base and propagates upwards to a depth of around 7 m, above which peak strain values still increase with similar slopes.

Figure 8. Incremental maximum shear strain in loose sand mobilised with wall translation: (a) from 0 to 0.1% *H*; (b) from 0.1% *H* to 0.2% *H*; (c) from 0.7% *H* to 0.8% *H*; (d) from 0.9% *H* to 1% *H*

Figure 9. Relationship between wall translational displacement and peak value of maximum shear strain in (a) loose sand; (b) dense sand

Figure 10 shows the deformation mechanism mobilised with wall translation in dense sand, which consists of two parts and is similar to that in loose sand. It can be seen from Figure 10(a) that a zone of sand behind the wall moves nearly vertically downwards as a column. Compared with that caused by wall rotation about the base as shown in Figure 5(a), the horizontal component of sand displacements behind the wall is higher and approximately uniform along the depth in accordance with the translational wall movement type. The sand column shears the sand on its left side with a prominent shear band with peak shear strain of 120% developing across the whole depth as shown in Figure 10(d). Figure 10(b), correspondingly, shows a vertical band with large dilative volumetric strain caused by the local sand collapse. Additionally, a shallow shear zone with approximately uniform strain values always exists at lower depths and a tiny sand core moves above it as assumed by Coulomb (1776). A calculation for the entire image sequence shows the prominent shear band caused by local collapse remains vertical while the average slope of the shallow shear zone increases from 52.9° to 58.3° with wall displacement, approximately matching the predictions of Bransby (1972) and Mayniel (1808) with calculated values of 53.3° and 64.2°, respectively.

The calculation also shows the two shear parts developing simultaneously at the beginning of wall translation, different from the behaviour observed in loose sand. One possible reason for this may be the compacted arrangement of sand grains, which are released instantly to fill the gap once the wall translates a very small displacement. The collapse of sand grains mobilises large shear strain behind the wall, which increases approximately linearly with wall translation as shown in Figure 9(b). It is noticeable that there is a sudden leap of peak strain values at all depths when the wall translates 0.36% H, which is the moment when the sand column fully forms and drops downwards dramatically according to the vectorial displacement measurement.

Figure 10. Dense sand deformation mobilised with wall translation: (a) vectorial displacement (scale=3); (b) volumetric strain (%); (c) and (d) maximum shear strain (%)

SAND DEFORMATIONS WITH WALL ROTATION ABOUT THE TOP

The rigid retaining wall can be rotated about its top by retracting only the lower pistons. During this process it can be seen from Figure 11(d) that a shear zone consisting of two parts is mobilised in loose sand, similar to that induced by wall translation. Figure 11(a) shows a rigid sand block behind the wall moving down and causing a primary shear zone across the whole depth all the way. A calculation for the entire image sequence indicates that the average slope of this zone increases from 45° initially to around θ_{inc} presented by Mayniel (1808). Additionally, a secondary shear band with relatively large strains originates from the wall base to nearly the surface and inclines at an angle of approximately $45°+\phi$ to the horizontal.

Figure 11. Loose sand deformation mobilised with wall rotation about the top: (a) vectorial displacement (scale=5); (b) volumetric strain (%); (c) and (d) maximum shear strain (%)

Wall rotation about the top limits sand movement at lower depths but provokes sand collapse in deeper layers, which is different from an approximately horizontally-uniform moving pattern caused by wall translation. It can thus be seen from Figure 11(a) that the much narrower rigid block is more like a long vertical strip instead of the triangular wedge in Figure 7(a). It is also worth noting that the slope of the curved shear zone in Figure 11(d), converse to that induced by wall translation, increases at lower stress levels, which is also a result of the horizontal constraint for sand in shallow layers. The shear zone exhibits dilative volumetric strain as shown in Figure 11(b) due to the slightly dilative behaviour of loose sand. Such wall movement also causes initiation of the secondary shear band with high strain at a very early stage, verified by the fact that there is nearly no coincidence of peak strain values at different depths in Figure

12(a). It can be consequently concluded that the upwards developing local collapse dominates the deformation mechanism mobilised with wall rotation about the top in loose sand.

Figure 12. Relationship between wall rotational displacement and peak value of maximum shear strain in (a) loose sand; (b) dense sand

Figure 13 shows the deformation mechanism mobilised with wall rotation about the top in dense sand, which ended at a small wall base displacement of 0.25% *H* because dense sand reaches the active state at lower displacement than loose sand. Similar to the deformation mechanism in loose sand, a rigid sand block moves above a shear zone across the whole depth with an inclination angle of 59.0°, which is approximately predicted by Equation 10 (Mayniel, 1808). Shear strain mobilised at depths less than 6 m is approximately uniform with depth, as can be seen from Figure 12(b), but greater at deeper levels. Local collapse originates from the wall base simultaneously and causes a vertical shear band with higher strain inclining at $45°+\phi$ to the horizontal. An obvious dilative band is also observed correspondingly as shown in Figure 13(b). However, the local shear band just develops to a depth of 2/3 wall height due to the small wall displacement, which is different from that running through nearly the whole depth in loose sand.

Figure 13. Dense sand deformation mobilised with wall rotation about the top: (a) vectorial displacement (scale=50); (b) volumetric strain (%); (c) and (d) maximum shear strain (%)

Comparison with the mechanism suggested by Bolton and Powrie (1988) as shown in Figure 1(b) reveals this mechanism to not capture the fundamental deformation processes occurring. In particular, while the mechanism proposes strain to largely occur within the triangle *ABO*, in fact the majority of the strains are in triangle *AVO*.

A SIMPLIFIED SAND DEFORMATION MECHANISM WITH WALL ROTATION ABOUT THE TOP

Analysis of the behaviour of flexible retaining walls in a manner similar to that attempted by Deng et al (2019) and Diakoumi & Powrie (2013) requires a link between the movement of the wall and the strains occurring in the soil. The experiments described here have given full-field measurements of the soil deformations and strains, but in order to calculate equivalent strains for flexible walls by superposition, a mathematical model coupling the soil deformations to the wall movements is necessary. As shown above, the mechanism proposed by Bolton and Powrie (1988) is inadequate when considering rotation about the wall top, a new mechanism will hence be developed here. While sands change volume during shearing, this process is complex and cannot be characterised by a constant dilation angle at all strains. The simplest approach to achieving an approximate mechanism for use in further analysis is thus to assume a zero-dilation mechanism which will be valid at critical state and approximately valid at lower displacements.

A simplified deformation mechanism for sand behind a rigid wall rotating about the top is proposed in Figure 14 based on the centrifuge test results shown in Figure 11. The mechanism comprises of a rigid sand block *ORV* which rotates with the wall and slides downwards and a deforming block *OAR* whose boundaries *OA* and *OR* incline at 45° and 45°+ϕ to the horizontal, respectively. A slip surface is assumed between the two blocks in order to simulate the local shear band originating from the wall base and developing nearly to the sand surface. It is noticeable that the sand displacement discontinuity starts from point *O* and ends at point *R* so that the sand surface *AV* is always continuous.

Figure 14. Simplified sand deformation mechanism with wall rotation about the top: (a) overall deformation mechanism; (b) sand settlement on a horizontal section; (c) an element in the deforming block

It can be seen from Figure 14(a) that the rigid block *ORV*, labelled as zone II, is assumed to move in a combined mode of vertical translation with a settlement of v_0 and anticlockwise rotation about point *V* with an outward angle of $\delta\theta$. The corresponding displacement field is presented in *x*-*y* coordinates with the origin at point *V* in Table 4. Additionally, the centrifuge test results show both horizontal and vertical displacements in zone I being approximately linear in the vertical direction *y* and quadratic in the horizontal direction *x*. Assuming the vertical displacement of a point at a depth of *y* on the boundary *OR* of zone I being $v'(y)$, the corresponding displacement field can thus be also described in Table 4.

As the vertical displacement along *AR* is parabolic, the average surface settlement in zone I is 1/3 of the maximum value. From volume conservation the vertical translational displacement v_0 can be calculated through Equation 11 as the area swept by the wall movement must be equal to the settlement of the sand surface.

$$v_0\alpha h + \frac{1}{2}\delta\theta\alpha^2 h^2 + \frac{1}{3}(1-\alpha)h(v_0 + \delta\theta\alpha h) = \frac{1}{2}\delta\theta h^2 \tag{11}$$

where v_0 is the vertical translational displacement of the rigid block *ORV*, h is the wall height, α is the width ratio of the rigid block *ORV* to the whole moving body *OAV* and $\delta\theta$ is the outward wall rotation angle.

Figure 14(b) shows the sand settlement at a depth of *y* and the displacement discontinuity at point *P* on the slip surface. The settlement of the horizontal section *QS* equals to the area swept by part of the wall *SO* so that $v'(y)$ can be calculated through Equation 12. It is worth noting

that the vertical displacement of point *R*, $v'(0)$, calculated by Equation 12 is equal to $v_0 + \delta\theta\alpha h$ so that the displacement discontinuity ends at the sand surface.

$$v_0\alpha(h-y) + \frac{1}{2}\delta\theta\alpha^2(h-y)^2 + \frac{1}{3}(1-\alpha)(h-y)v'(y) = \frac{1}{2}\delta\theta(h^2-y^2) \qquad (12)$$

Although dilative strain was observed in loose sand as shown in Figure 11(b), volumetric strain is always assumed as zero everywhere in the simplified mechanism. The zero volumetric strain in an element in zone I as shown in Figure 14(c) results in Equation 13, which can be used for calculating the horizontal displacement.

$$u_{(i,j-1)} - u_{(i,j)} + u_{(i+1,j-1)} - u_{(i+1,j)} = v_{(i,j-1)} + v_{(i,j)} - v_{(i+1,j-1)} - v_{(i+1,j)} \qquad (13)$$

Table 4. Displacements mobilised with wall rotation about the top and base

Wall movement type	Zone	Horizontal displacement, u	Vertical displacement, v
Rotation about the top	I	$f[v(x,y)]$	$\left[\frac{h-x-y}{(1-\alpha)(h-y)}\right]^2 v'(y)$
Rotation about the top	II	$-y\delta\theta$	$x\delta\theta + v_0$
Rotation about the base	--	$-(h-x-y)\delta\theta$	$(h-x-y)\delta\theta$

In order to validate such a mechanism, wall rotation about the top with a wall base displacement of 2% *H* was simulated with corresponding displacement and strain distributions being shown in Figures 15(b) and 16(a). It can be seen that the mechanism gives a good prediction of the centrifuge test results shown in Figures 15(a) and 11(d), respectively, with both the resultant sand displacements and maximum shear strain being reasonably well matched.

Figure 15. Comparison of measured and predicted sand displacements:

(a) and (b) measured and predicted displacements for wall rotation about the top (wall base displacement = 2% *H*);

(c) and (d) measured and predicted displacements for wall translation (wall displacement = 1% *H*)

SUPERPOSITION OF MECHANISMS WITH WALL ROTATION ABOUT THE TOP AND BASE

Bolton and Powrie (1988) proposed a hypothesis that the admissible strain field caused by outward wall translation can be determined by the superposition of those compatible with equal but opposite wall rotation about the base and top. Bolton and Powrie (1988) assumed that the strains due to wall rotation about the top all occurred in the triangle *ABO*, however the centrifuge test results reveal that the majority of strains actually occurred in *AVO*. A direct superposition of shear strains within *AVO* may not make sense owing to different principal directions so the superposition of displacements was conducted.

In order to predict the sand deformation mobilised with wall translation, the deformation mechanism for wall rotation about the base proposed by Bolton and Powrie (1988) and validated by centrifuge tests was utilised. Sand moves and shears in the deforming zone *AVO* with the hypotenuse inclining at 45° to the horizontal as shown in Figure 1(a). The centrifuge test results show linear distributions of horizontal and vertical displacements so that the displacement field is proposed as shown in Table 4.

The displacement fields compatible with equal but opposite wall rotation about the base and top were superposed with the consequent resultant displacement and maximum shear strain being presented in Figures 15(d) and 16(b). Compared with observed results shown in Figures 15(c) and 7(d), it can be concluded that such a superposition of two simplified mechanisms can impressively predict the sand deformation mobilised with wall translation.

Figure 16. Sand maximum shear strains mobilised with: (a) wall rotation about the top (wall base displacement = 2% *H*); (b) wall translation (wall displacement = 1% *H*)

The ability to adequately predict the strain distribution behind retaining walls at pre-failure states gives the possibility of performing mobilisable strength design following the methods proposed by Deng et al. (2019) for retaining walls in clay. Linking the wall displacements to the soil strains through the analyses presented here and hence to earth pressures by utilising a simplified constitutive law allows a deformed shape in which the earth pressures are in equilibrium with the wall bending moments to be achieved by iteration.

CONCLUSIONS

Conventional retaining wall design in sand is based on ultimate limit state analysis together with arbitrary factors of safety, while wall movement is often estimated through separate serviceability limit state calculation due to a lack of accurate but simple deformation mechanisms. This paper has presented an experimental study of the sand deformations mobilised with a complete set of active wall movement modes and then proposed a simplified deformation mechanism for sand behind a rigid wall rotating about the top.

The simplified mechanism has been shown to achieve a good prediction for observed sand deforming behaviours in centrifuge tests. The sand deformation caused by wall translation has been well characterised by the superposition of mechanisms with wall rotation about the top and base.

The simplified deformation analyses, together with a sand constitutive model, could be used to predict earth pressure behaviours mobilised with retaining wall movement. This work thus should make it possible to design retaining walls in sand with simultaneous consideration of safety and serviceability in a single calculation.

REFERENCES

Adrian, R. J. (1991). Particle-imaging techniques for experimental fluid mechanics. *Annual review of fluid mechanics* **23**, No. 1, 261-304.

Arthur, J. (1962). Strains and lateral force in sand. PhD thesis, *Cambridge University*

ASTM. (2011). Method for consolidated drained triaxial compression test for soils. *D 7181, Annual Book of Standards*, *4*.

Bolton, M. (1986). Strength and dilatancy of sands. *Géotechnique* **36**, No. 1, 65-78.

Bolton, M. & Powrie, W. (1988). Behaviour of diaphragm walls in clay prior to collapse. *Géotechnique* **38**, No. 2, 167-189.

Bransby, P. (1972). General theories of earth pressures and deformations. *Proc. of European Conference on Soil Mechanics.* **2**, 75–78.

Bransby, P. & Milligan, G. (1975). Soil deformations near cantilever sheet pile walls. *Géotechnique* **25**, No. 2, 175-195.

Bransby, P. L. (1968). *Stress and strain in sand caused by rotation of a model wall.* University of Cambridge.

Chang, C. S. & Chao, S.-J. (1994). Discrete element analysis for active and passive pressure distribution on retaining wall. *Computers and Geotechnics* **16**, No. 4, 291-310.

Coulomb, C. (1776). An attempt to apply the rules of maxima and minima to several problems of stability related to architecture. *Mémoires de l'Académie Royale des Sciences* **7**, No., 343-382.

Deng, C. & Haigh, S. (2018). Soil movement mobilised with retaining wall rotation in loose sand. *Physical Modelling in Geotechnics, Volume 2.* CRC Press.

Deng, C., Haigh, S.K., Ma, X. and Xu, J. (2019). A design method for flexible retaining walls in clay. *Géotechnique*, pp.1-10.

Deng, C. (2020). *Sand Deformation Mechanisms and Earth Pressures Mobilised with Retaining Wall Movements.* PhD thesis, University of Cambridge, UK.

Diakoumi, M. and Powrie, W. (2013). Mobilisable strength design for flexible embedded retaining walls. *Géotechnique* **63**, No. 2, 95–106.

Fang, Y.-S., Chen, T.-J. & Wu, B.-F. (1994). Passive earth pressures with various wall movements. *Journal of Geotechnical Engineering* **120**, No. 8, 1307-1323.

Fang, Y.-S. & Ishibashi, I. (1986). Static earth pressures with various wall movements. *Journal of Geotechnical Engineering* **112**, No. 3, 317-333.

Gautier, H. (1717). *Dissertation sur l'epaisseur des culées des ponts*, Chez André Cailleau.

Haigh, S.K., Eadington, J. & Madabhushi, S.P.G. (2012) Permeability and stiffness of sands at very low effective stresses. *Géotechnique* **62**, No. 1, 69-75.

Lau, C. & Bolton, M. (2011). The bearing capacity of footings on granular soils. I: Numerical analysis. *Géotechnique* **61**, No. 8, 627-638.

Lesniewska, D., Niedostatkiewicz, M. & Tejchman, J. (2012). Experimental study on shear localisation in granular materials within combined strain and stress field. *Strain* **48**, 430-444.

Lord, J. (1969). *Stresses and strains in an earth pressure problem.* PhD thesis, University of Cambridge.

Madabhushi, S., Houghton, N. & Haigh, S. (2006) A new automatic sand pourer for model preparation at University of Cambridge. Proceedings of the 6th International Conference on Physical Modelling in Geotechnics, 2006. Taylor & Francis Group, London, UK, 217-222.

Mayniel, J. H. (1808). *Traité expérimental, analytique et pratique de la poussée des terres et des murs de revêtement*, Bachelier librairie.

Mühlhaus, H.B. and Vardoulakis, I. (1987). The thickness of shear bands in granular materials. *Géotechnique* **37**, No. 3, 271-283.

Niedostatkiewicz, M., Lesniewska, D. & Tejchman, J. (2011). Experimental analysis of shear zone patterns in cohesionless for earth pressure problems using particle image velocimetry. *Strain* **47**, No., 218-231.

Potts, D. & Fourie, A. (1986). A numerical study of the effects of wall deformation on earth pressures. *International journal for numerical and analytical methods in geomechanics* **10**, No. 4, 383-405.

Rankine, W. J. M. (1857). II. On the stability of loose earth. *Philosophical transactions of the Royal Society of London* No. 147, 9-27.

Roscoe, K. (1963). The determination of strains in soils by an X-ray method. *Civ. Engng Publ. Wks Rev.* **58**, No., 873-876, 1009-1012.

Rowe, P. & Peaker, K. (1965). Passive earth pressure measurements. *Géotechnique* **15**, No. 1, 57-78.

Schofield, A. N. (1980). Cambridge geotechnical centrifuge operations. *Géotechnique* **30**, No. 3, 227-268.

Schanz, T. and Vermeer, P. (1996). Angles of friction and dilatancy of sand. *Géotechnique* **46**, No. 1, 145-151.

Smith, I. A. A. (1972). *Stress and strain in a sand mass adjacent to a model wall.* PhD thesis, University of Cambridge.

Stanier, S. A., Blaber, J., Take, W. A. & White, D.J. (2015). Improved image-based deformation measurement for geotechnical applications. *Canadian Geotechnical Journal* **53**, No. 5, 727-739.

White, D., Take, W. & Bolton, M. (2003). Soil deformation measurement using particle image velocimetry (PIV) and photogrammetry. *Géotechnique* **53**, No. 7, 619-631.

Figure 1

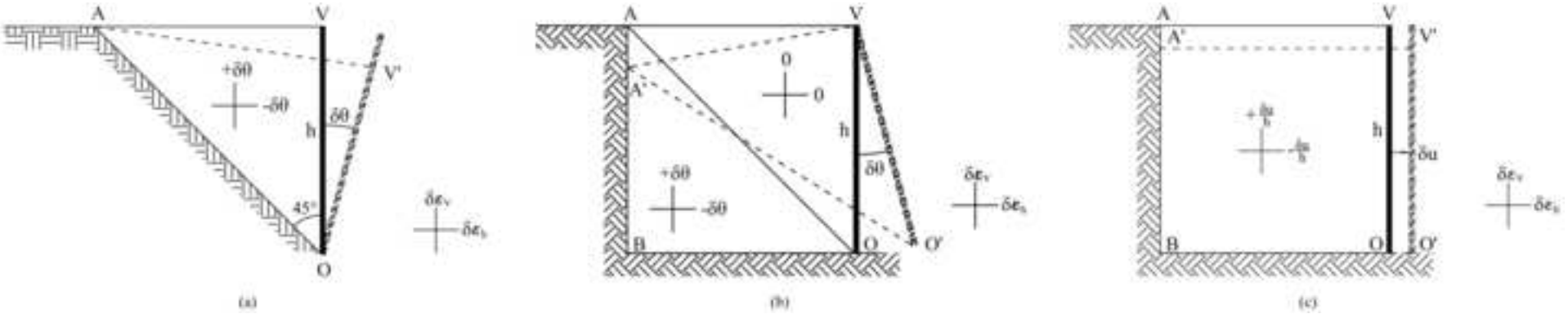

Background

Figure 2

Click here to access/download;Figure;Dengfig02.tif

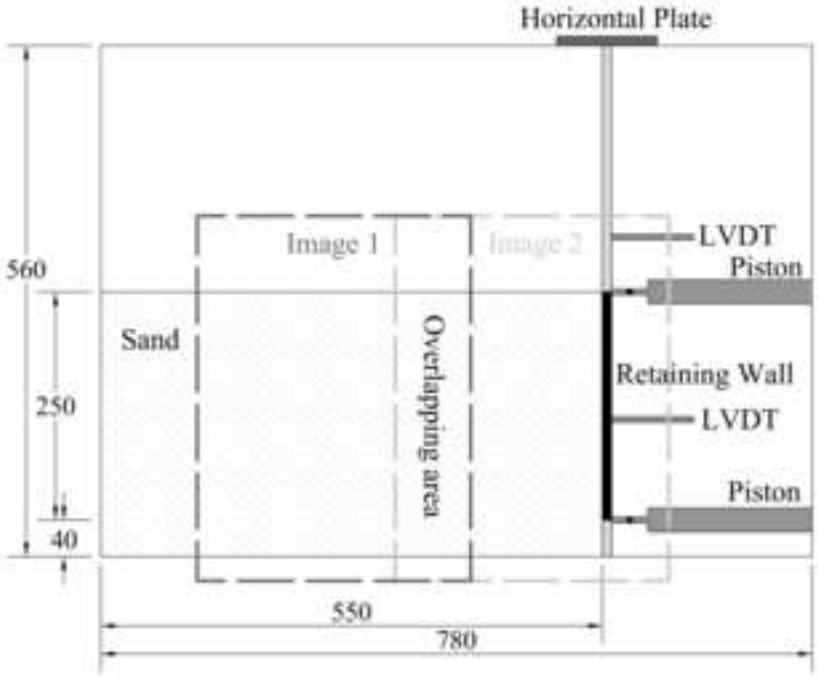

(a)

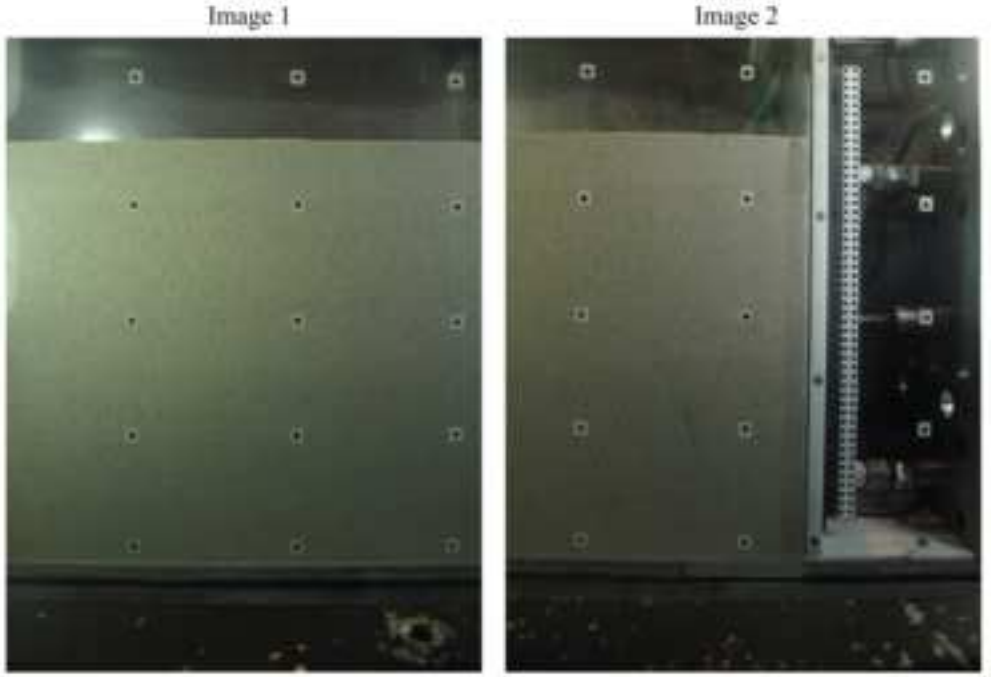

(b)

Fig. 2

Figure 3

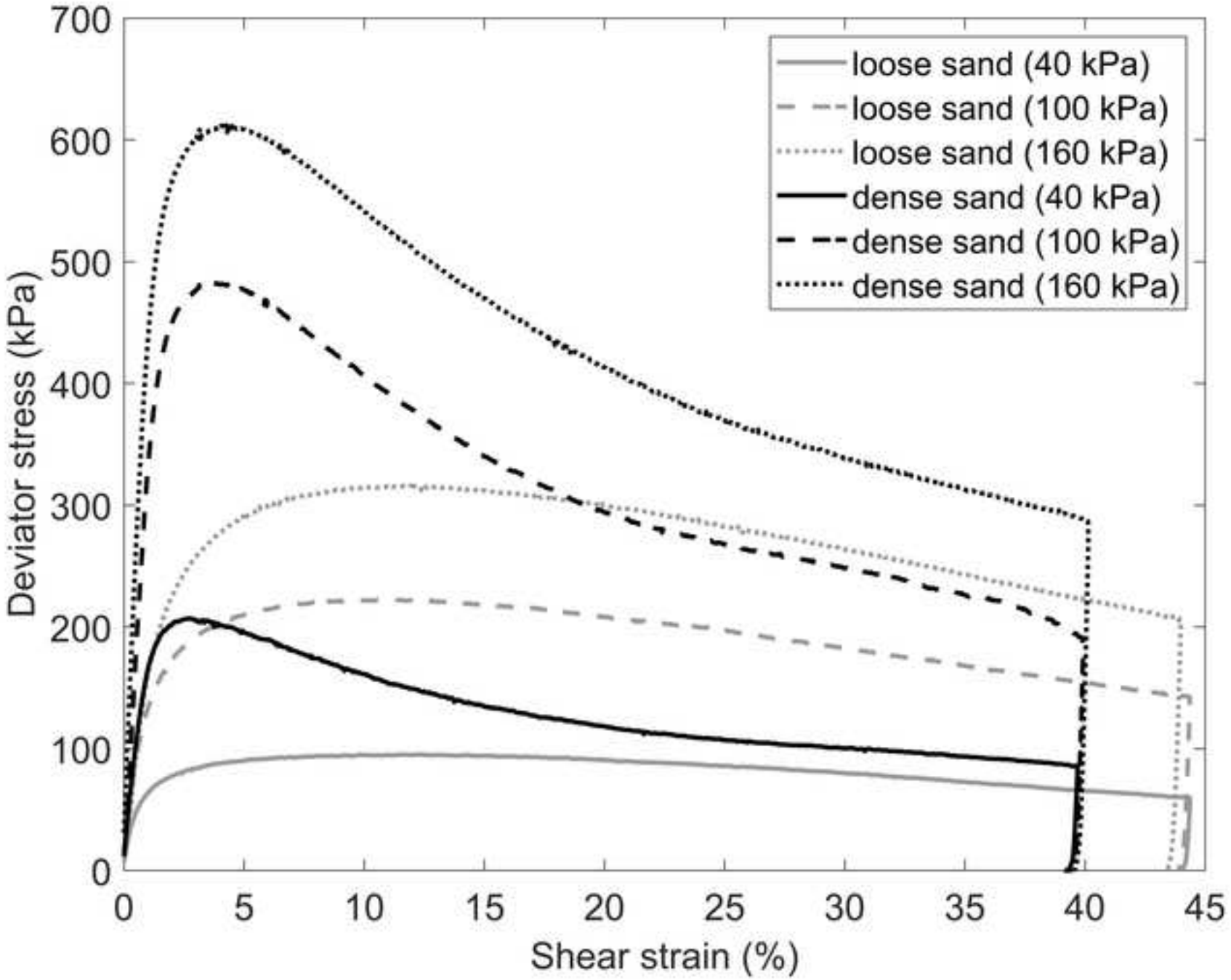

Figure 4

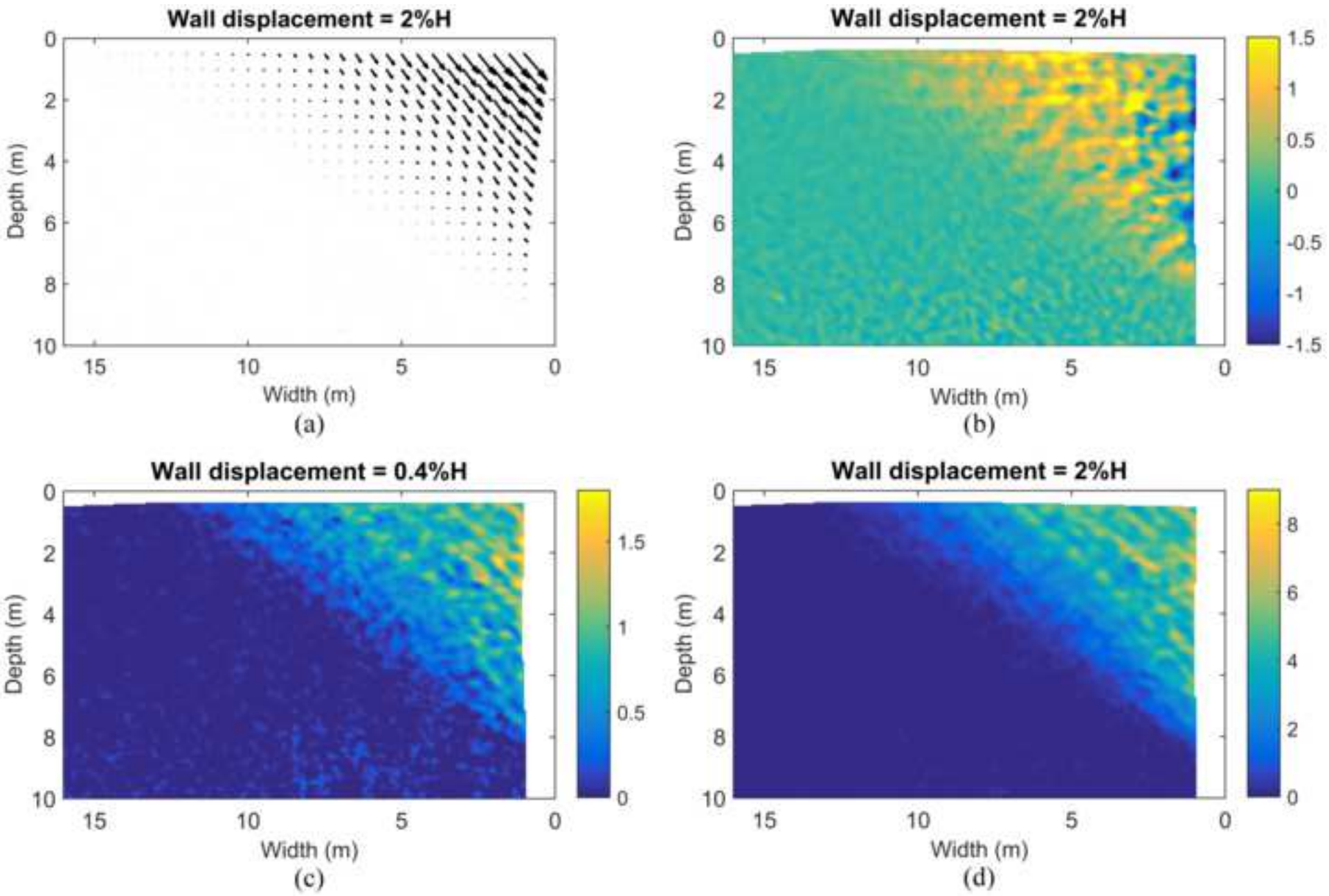

Figure 5

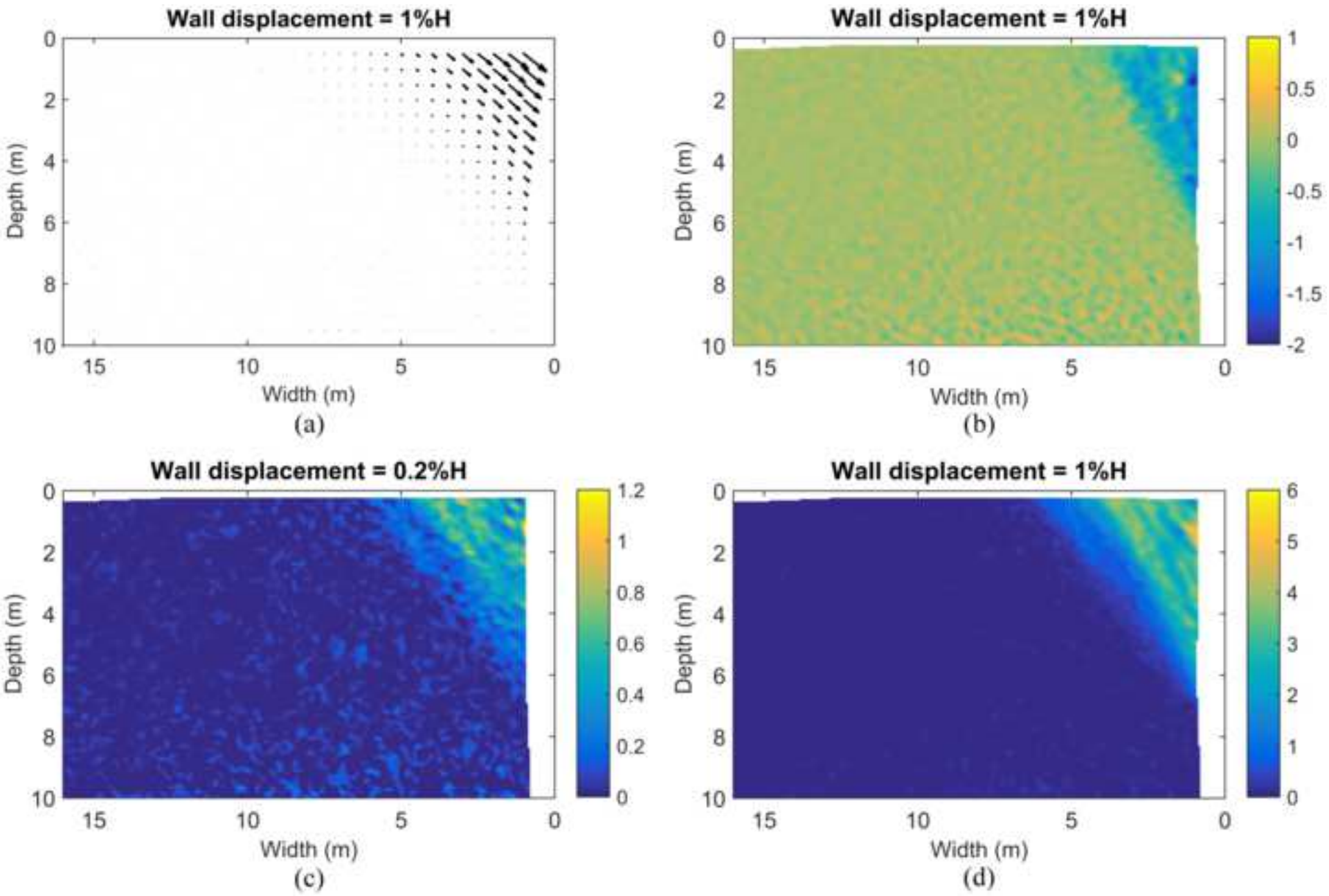

Figure 6

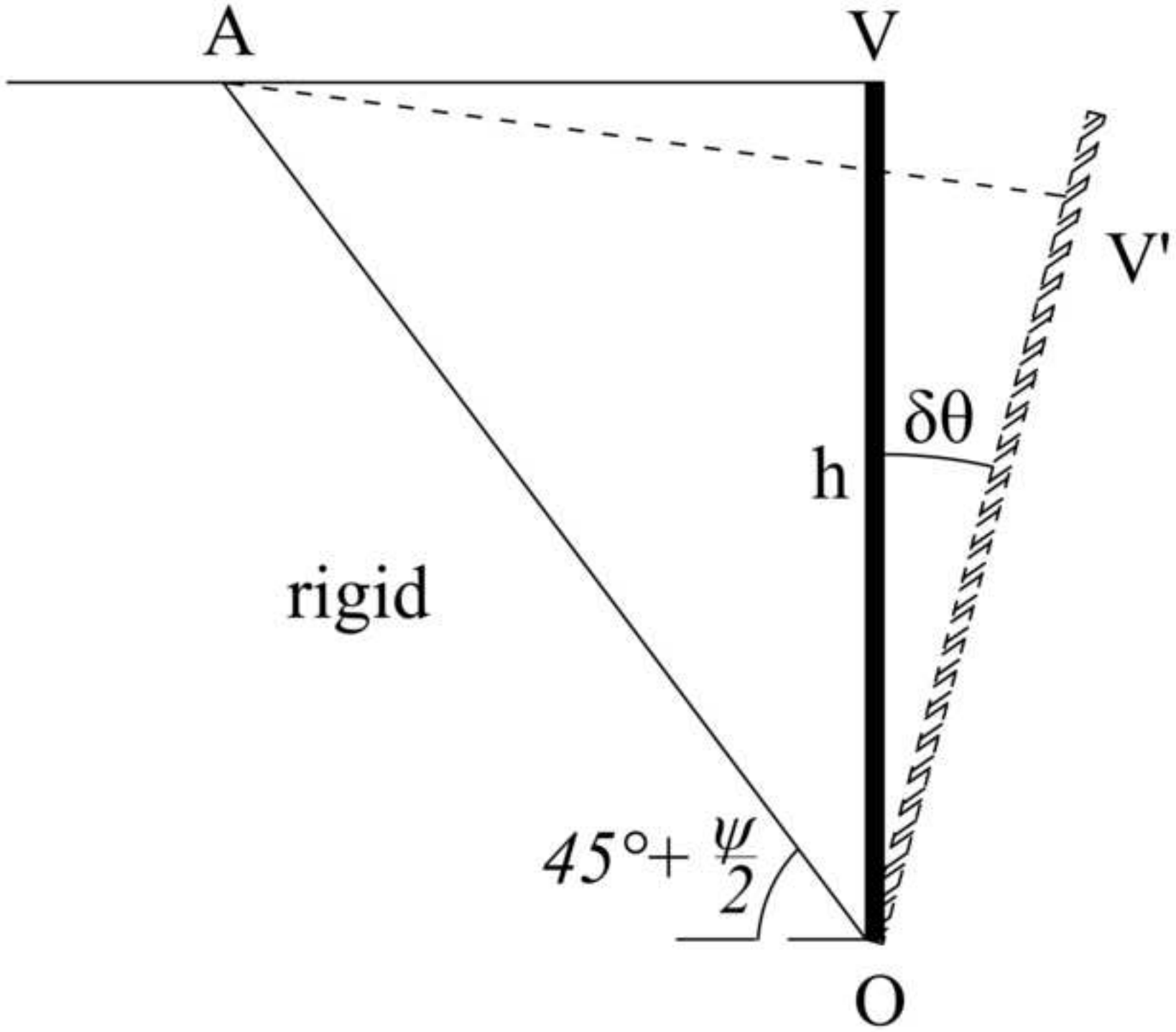

Figure 7

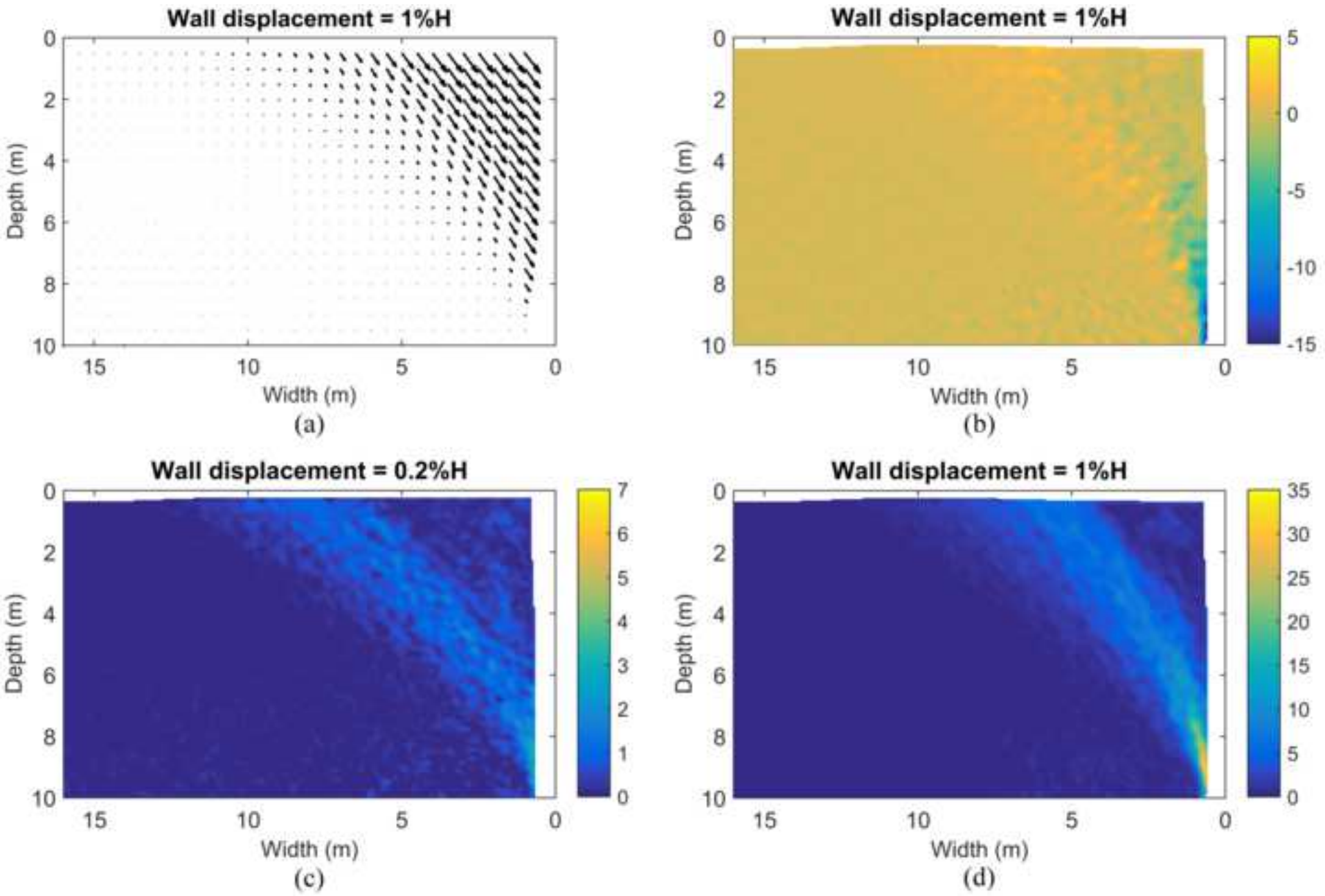

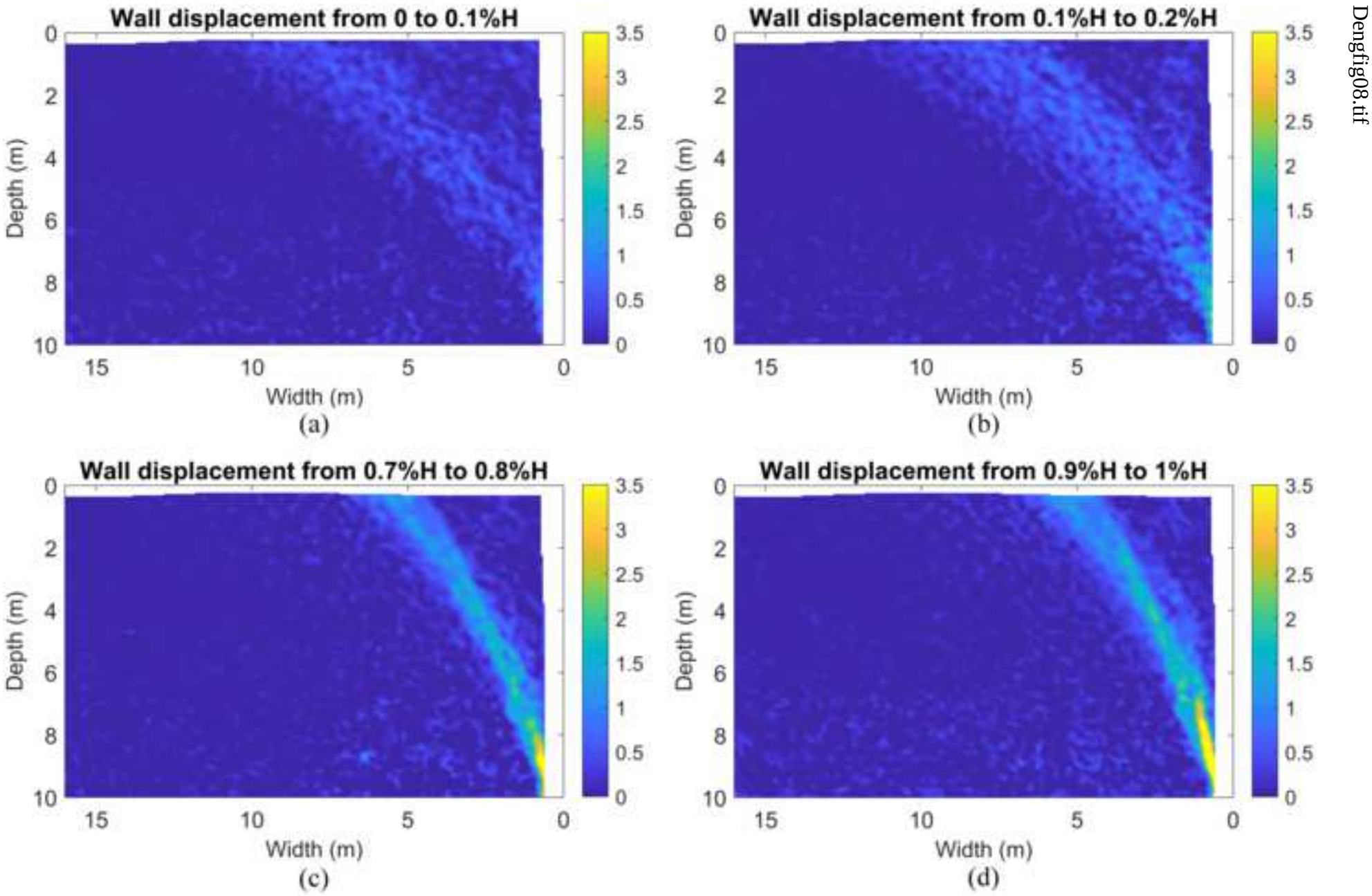

Figure 9

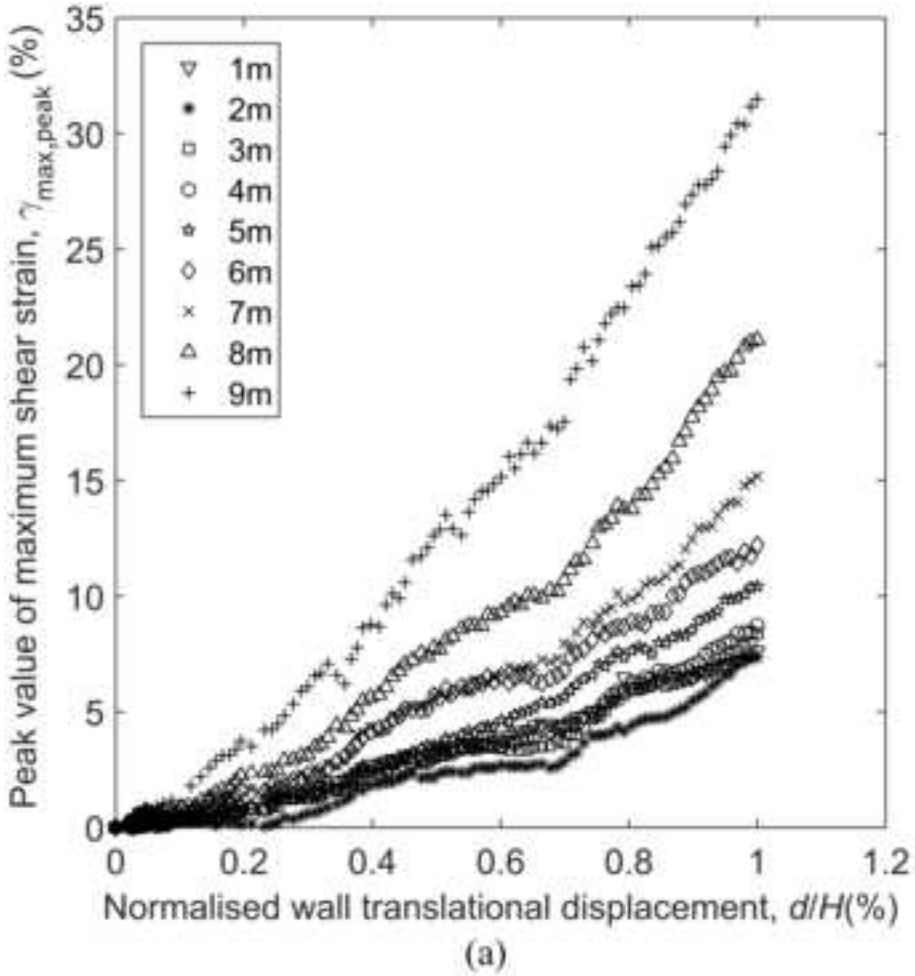

(a)

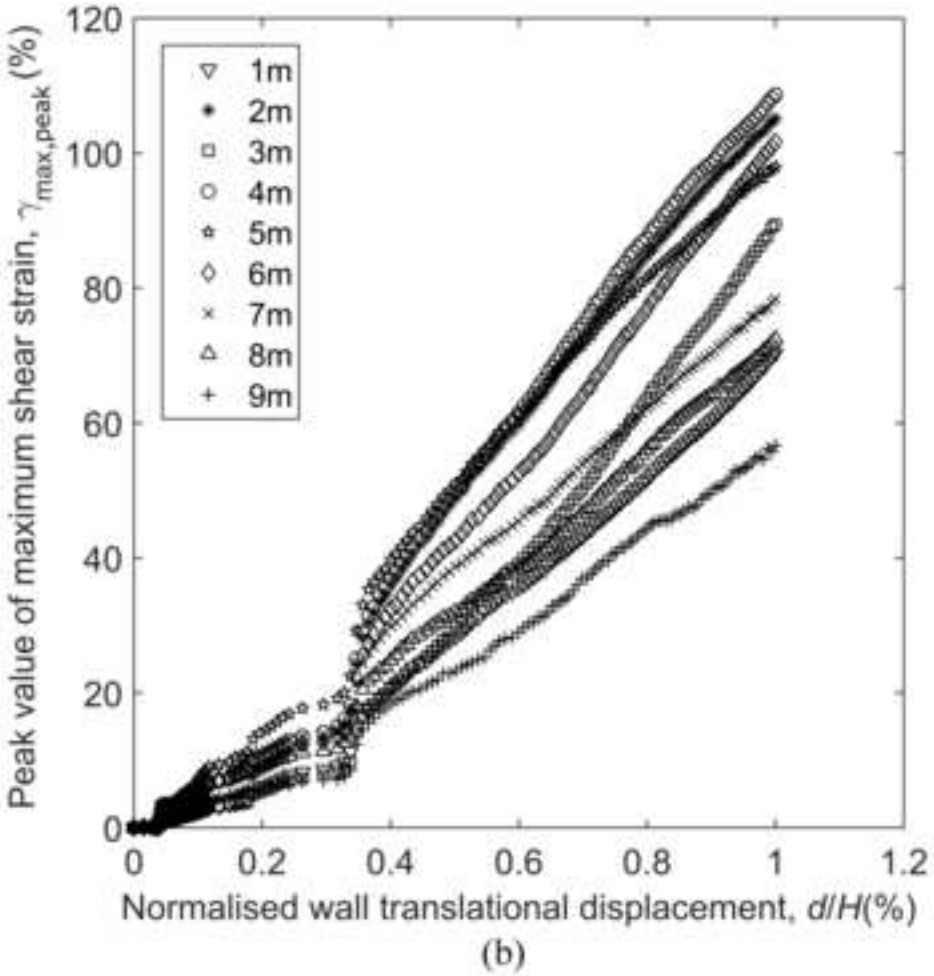

(b)

Dengfig08.tif

Figure 10

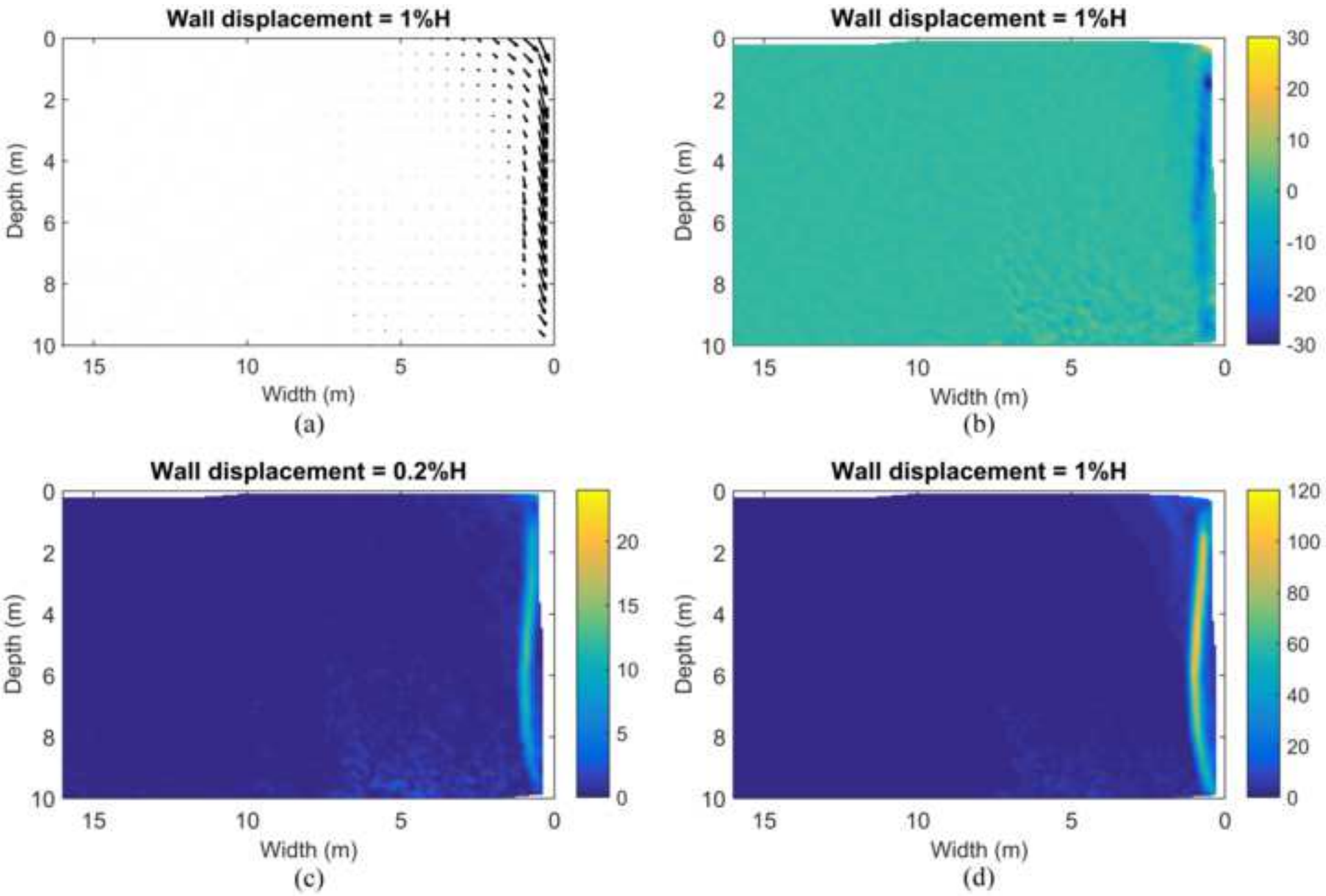

Figure 11

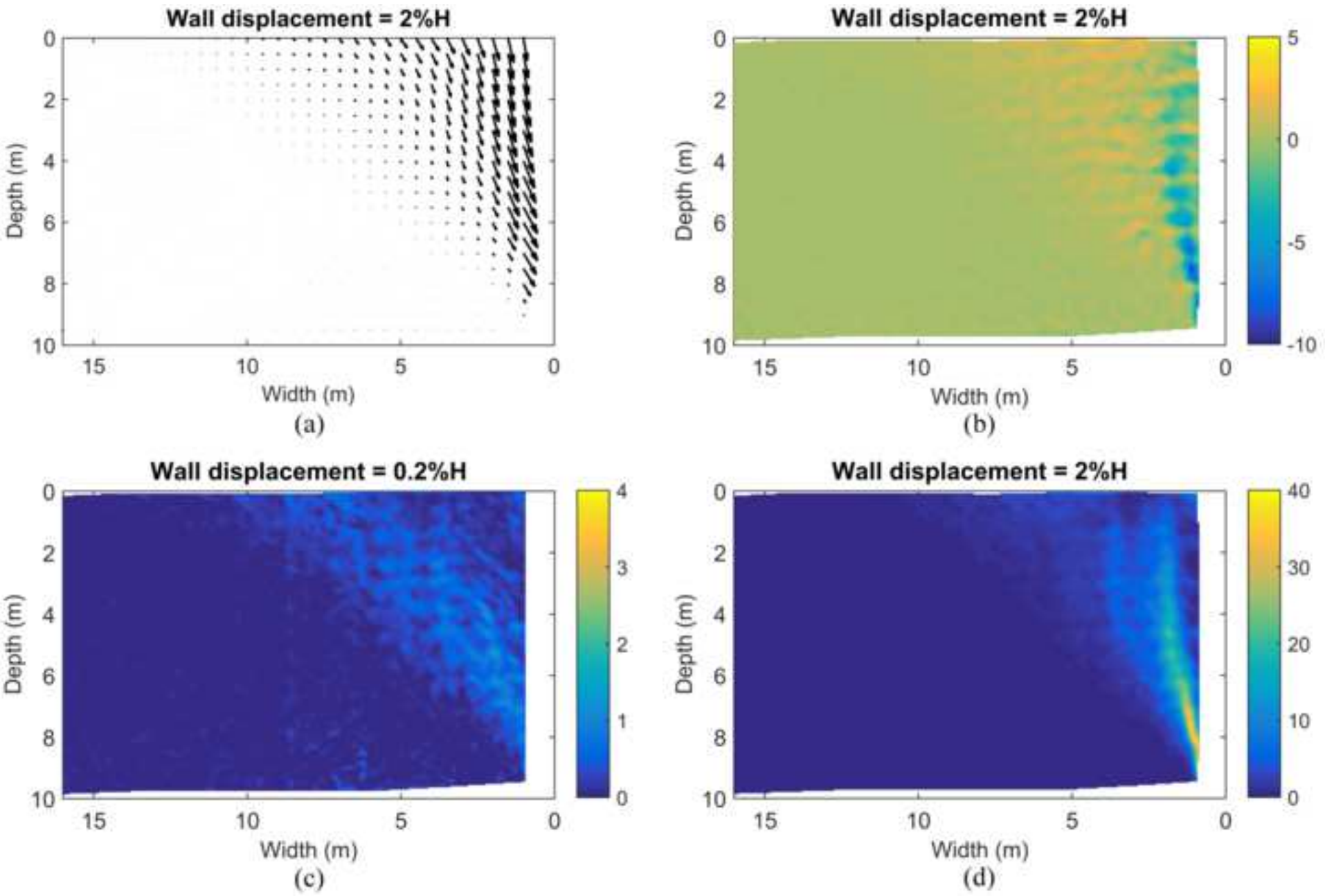

Figure 12

Click here to access/download;Figure;Dengfig12.tif

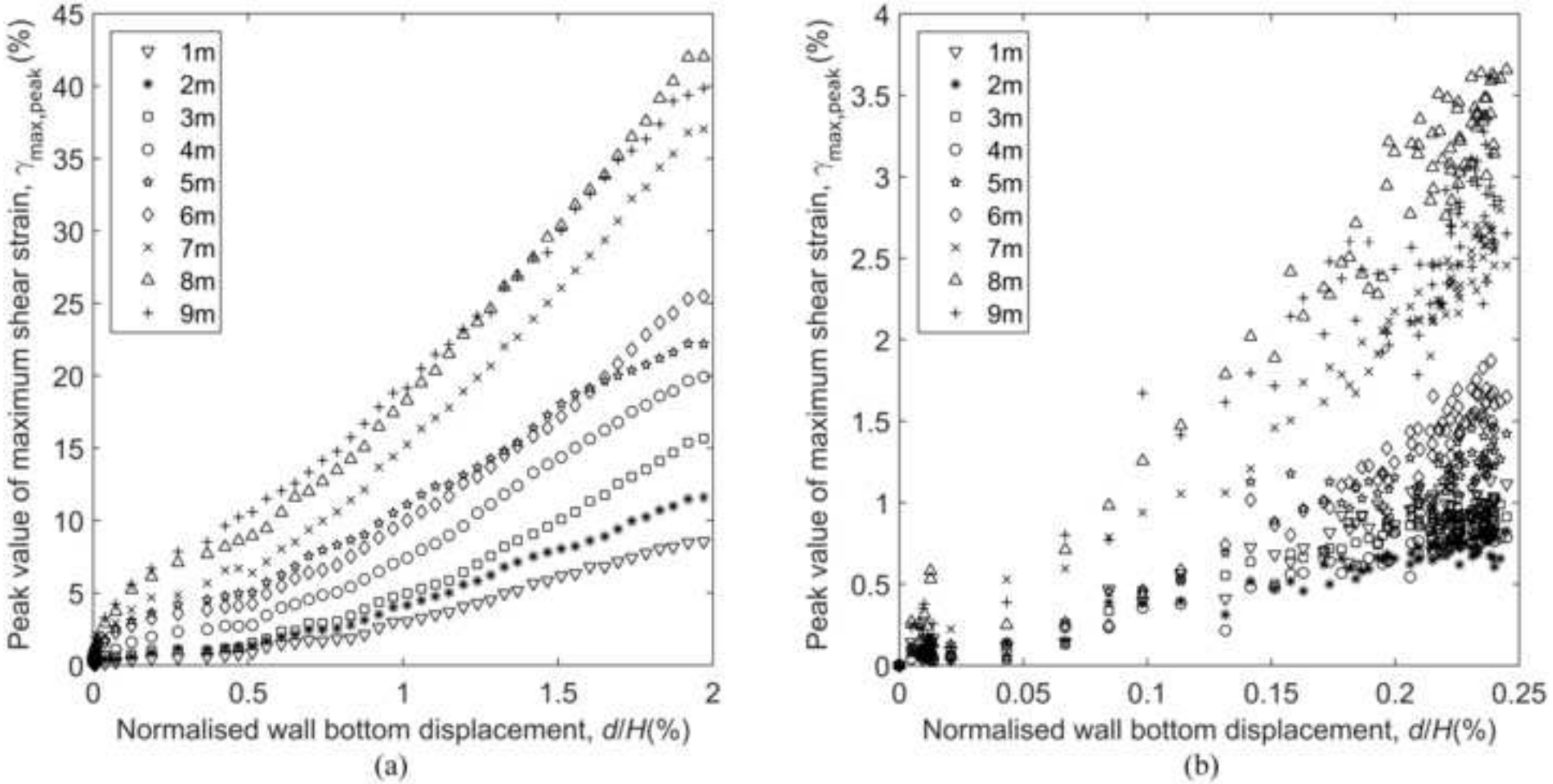

Dengfig13.tif

Figure 13

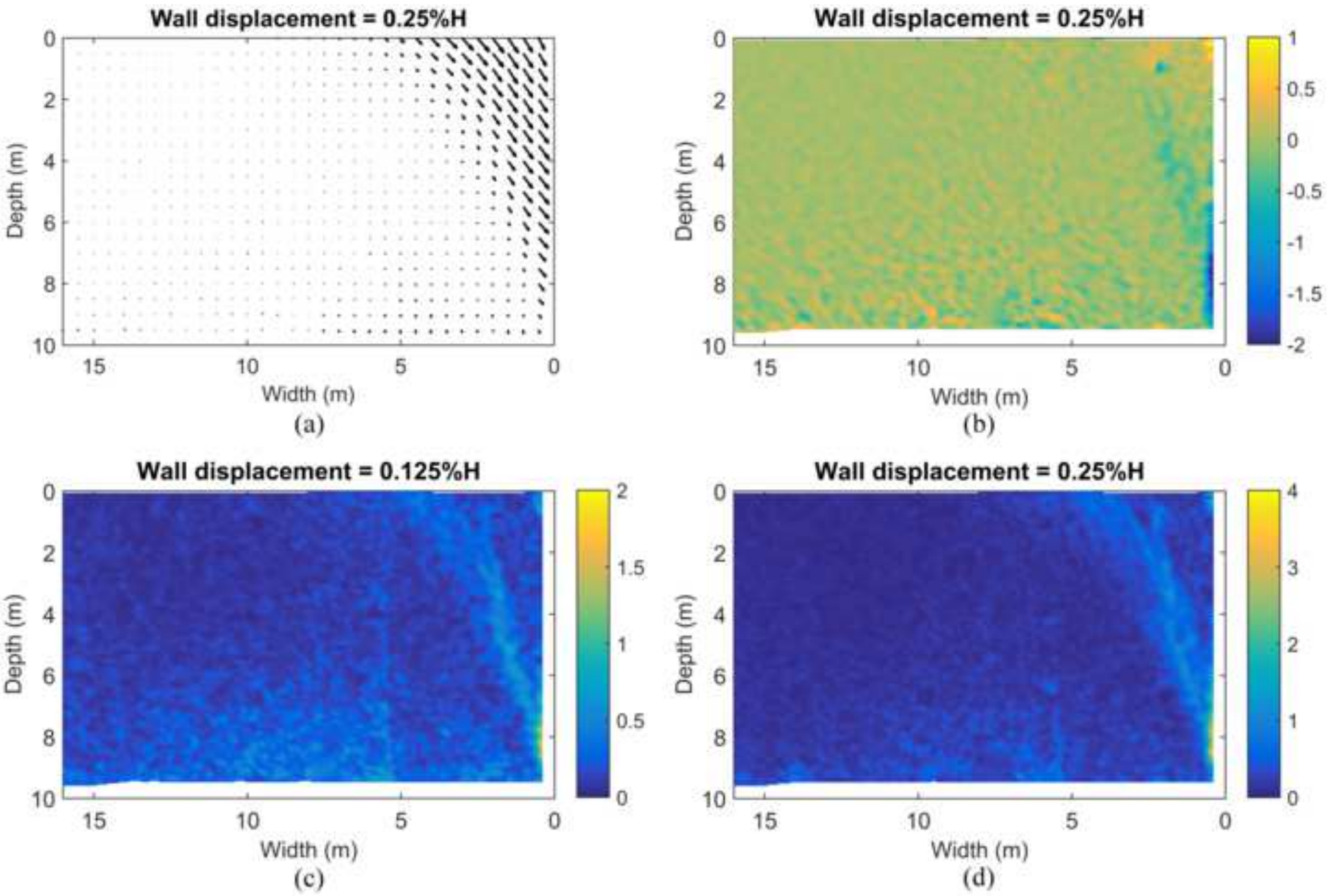

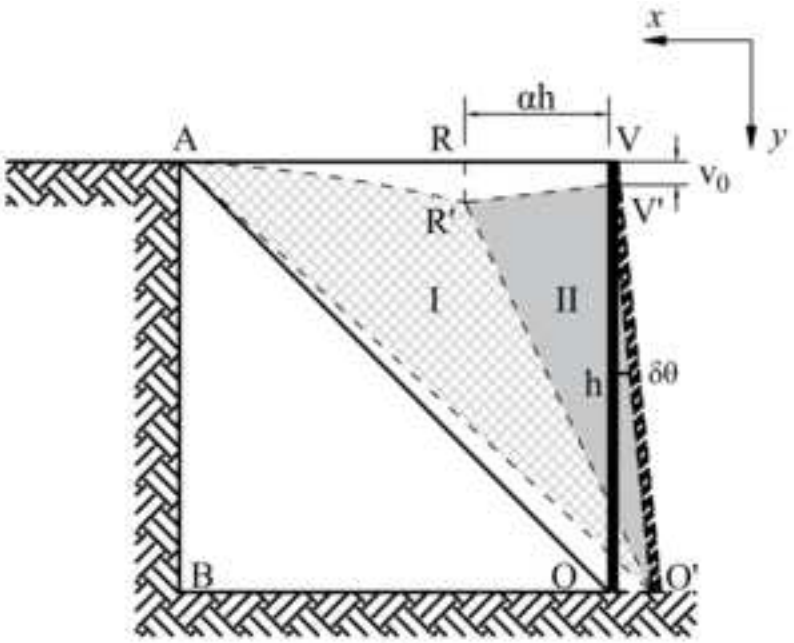

(a)

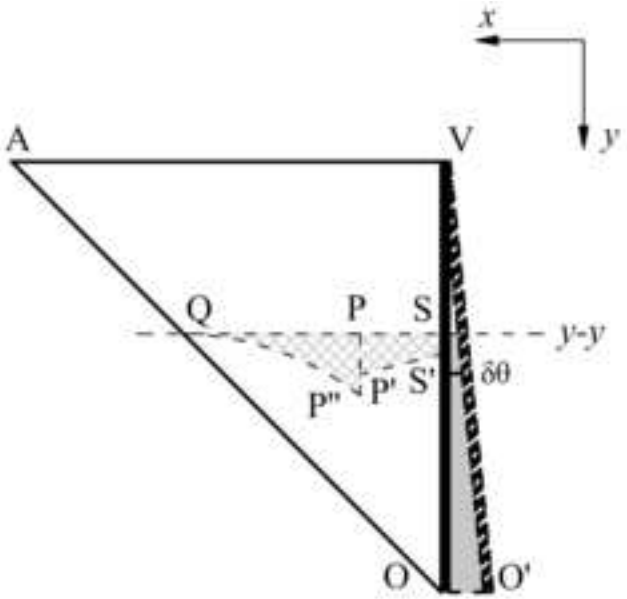

(b)

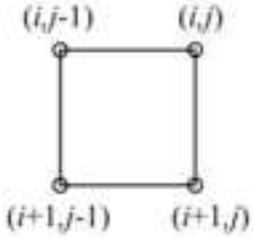

(c)

Figure 15

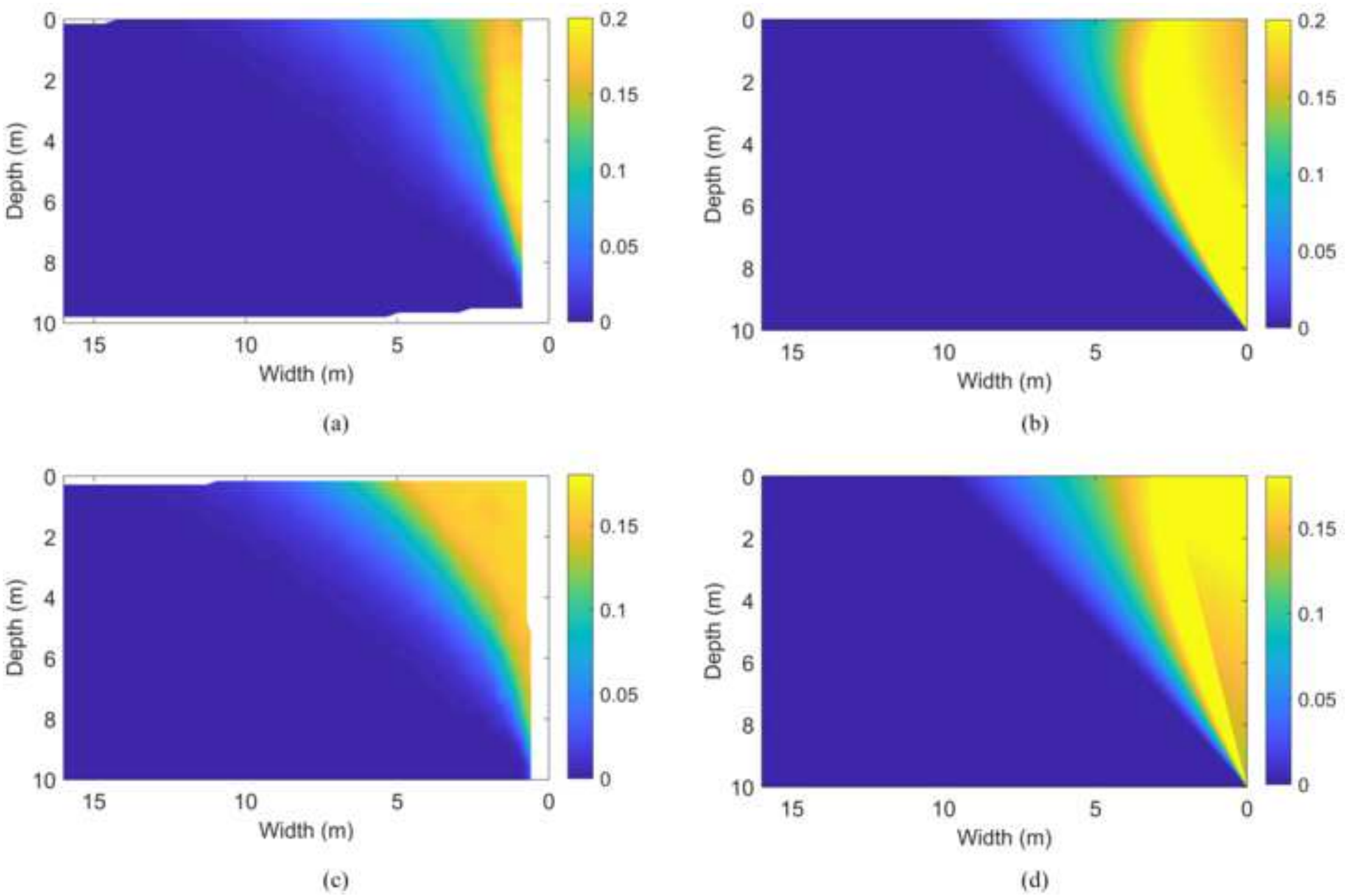

Figure 16

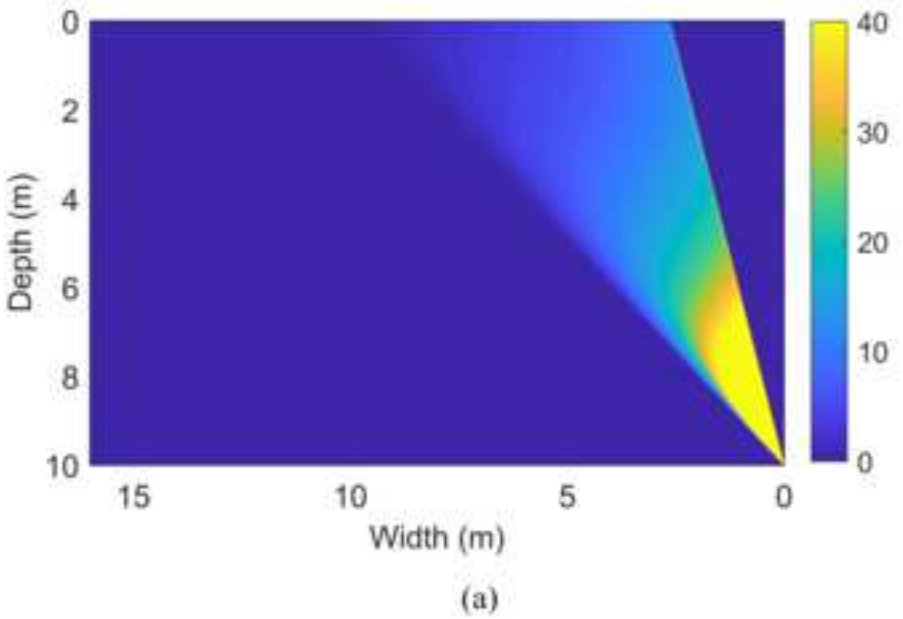

(a)

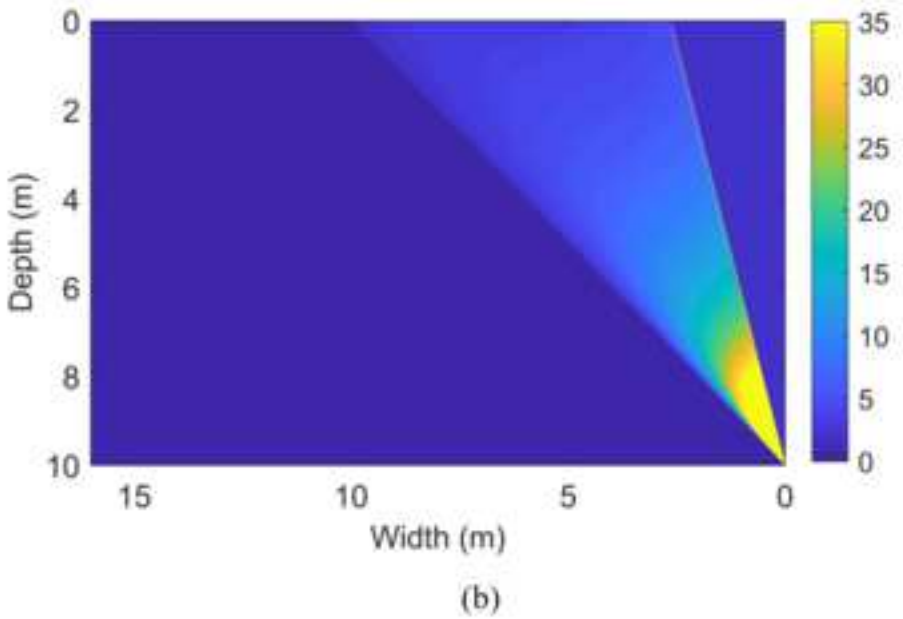

(b)

Dengfig14.tif

Notation

$\delta\theta$: the wall rotation angle increment (radian)

$\delta\varepsilon_h$: the horizontal strain increment of soil

$\delta\varepsilon_v$: the vertical strain increment of soil

$\delta\gamma$: the shear strain increment of soil

$\delta\varepsilon_{vol}$: the volumetric strain increment of soil

$e_{\max}$: the maximum void ratio of sand

$e_{\min}$: the minimum void ratio of sand

G_s: the specific gravity of solid

d_{50}: the average particle size of sand

ϕ: the friction angle of sand

ϕ_p: the peak friction angle of sand

ϕ_{crit}: the critical friction angle of sand

$\phi_{p,p}$: the predicted peak friction angle of sand

ψ: the dilation angle of sand

ψ_p: the peak dilation angle of sand

δ: the interface friction angle between sand and the wall

$\overline{\gamma_{max}}$: the average maximum shear strain of sand

$\gamma_{max,peak}$: the peak value of maximum shear strain of sand

H: the height of the retaining wall used in centrifuge tests

θ_{inc}: the inclination angle of the sliding surface

u: the horizontal displacement of sand

v: the vertical displacement of sand

Caption

Figure 1. Admissible strain fields for (a) wall rotation about the base; (b) wall rotation about the top; (c) wall translation (Bolton and Powrie (1988))

Figure 2. (a) Schematic diagram of experimental set-up; (b) Unprocessed images captured simultaneously

Figure 3. Stress-strain curves of Hostun sand

Figure 4. Loose sand deformation mobilised with wall rotation about the base: (a) vectorial displacement (scale=5); (b) volumetric strain (%); (c) and (d) maximum shear strain (%)

Figure 5. Dense sand deformation mobilised with wall rotation about the base: (a) vectorial displacement (scale=10); (b) volumetric strain (%); (c) and (d) maximum shear strain (%)

Figure 6. Shear wedge compatible with wall rotation about the base

Figure 7. Loose sand deformation mobilised with wall translation: (a) vectorial displacement (scale=5); (b) volumetric strain (%); (c) and (d) maximum shear strain (%)

Figure 8. Incremental maximum shear strain in loose sand mobilised with wall translation: (a) from 0 to 0.1% *H*; (b) from 0.1% *H* to 0.2% *H*; (c) from 0.7% *H* to 0.8% *H*; (d) from 0.9% *H* to 1% *H*

Figure 9. Relationship between wall translational displacement and peak value of maximum shear strain in (a) loose sand; (b) dense sand

Figure 10. Dense sand deformation mobilised with wall translation: (a) vectorial displacement (scale=3); (b) volumetric strain (%); (c) and (d) maximum shear strain (%)

Figure 11. Loose sand deformation mobilised with wall rotation about the top: (a) vectorial displacement (scale=5); (b) volumetric strain (%); (c) and (d) maximum shear strain (%)

Figure 12. Relationship between wall rotational displacement and peak value of maximum shear strain in (a) loose sand; (b) dense sand

Figure 13. Dense sand deformation mobilised with wall rotation about the top: (a) vectorial displacement (scale=50); (b) volumetric strain (%); (c) and (d) maximum shear strain (%)

Figure 14. Simplified sand deformation mechanism with wall rotation about the top: (a) overall deformation mechanism; (b) sand settlement on a horizontal section; (c) an element in the deforming block

Figure 15. Comparison of measured and predicted sand displacements: (a) and (b) measured and predicted displacements for wall rotation about the top (wall base displacement = 2% *H*); (c) and (d) measured and predicted displacements for wall translation (wall displacement = 1% *H*)

Figure 16. Sand maximum shear strains mobilised with: (a) wall rotation about the top (wall base displacement = 2% *H*); (b) wall translation (wall displacement = 1% *H*)

Table 1. Summary of test configurations

Table 2. Geotechnical properties of Hostun sand

Table 3. Strength and dilatancy parameters of Hostun sand

Table 4. Displacements mobilised with wall rotation about the top and base